Assimilation of L-band InSAR snow depth retrievals for improved snowpack quantification

Prabhakar Shrestha[1] and Ana P. Barros[1]

[1]Department of Civil and Environmental Engineering, University of Urbana-Champaign, Urbana, Illinois, USA.

Corresponding Author: Ana P. Barros (barros@illinois.edu)

Abstract

The integration of snow hydrology models and remote sensing observations via data assimilation is a promising method to capture the dynamics of seasonal snowpacks at high spatial resolution and reduce uncertainty with respect to snow water resources. In this study, we employ interferometric Synthetic Aperture Radar (InSAR) technique to quantify snow depth change using modeled snow density and assimilate the referenced and calibrated retrievals into a multilayer snow hydrology model (MSHM). Although the impact of assimilating snow depth change is local in space and time, the impact on snowpack mass properties (snow depth or SWE) is cumulative, and the InSAR retrievals are valuable to improve snowpack simulation and capture the spatial and temporal variability of snow depth or SWE. Details in the estimation algorithm of InSAR snow depth or SWE changes, referencing and calibration prove to be important to minimize errors during data assimilation.

1 Introduction

Remote sensing and distributed modelling of snowpack with data assimilation is a promising methodology to quantify snow water resources (including condition) and reduce uncertainty. Current and upcoming snow remote sensing using Synthetic Aperture Radar (SAR) aim to provide global coverage at hyper-resolution, which is needed to quantify snow variability with reduced uncertainty. Recent studies have either mostly used backscatter approaches (Lievens et al., 2019, 2022; Singh et al., 2024; Tsang et al., 2021) or interferometric SAR (InSAR) techniques(Guneriussen et al., 2001) to quantify snow depth and snow water equivalent (SWE). The latter have been applied extensively for SWE retrievals from dry snowpacks using ground-based (e.g. Leinss et al., 2015; Ruiz et al., 2022) and satellite-based SARs (e.g. Conde et al., 2019; Dagurov et al., 2020; Deeb et al., 2011; Guneriussen et al., 2001; Lei et al., 2023; H. Li et al., 2016; S. Li & Sturm, 2002; Liu et al., 2017). The InSAR technique assumes that the volume backscatter and absorption of microwave signal in the snowpack are negligible with the backscatter at the ground-snowpack interface being dominant while slow propagation of radar waves through snowpack (depending on dielectric property) results in phase delay. Previous studies have shown also that the InSAR retrievals are more suitable at longer wavelengths (e.g., L-band), owing to transparency of dry snow and forest over snow, preservation of coherence for longer periods of time and larger threshold for phase wrapping. With the upcoming NASA-ISRO (Indian Space Research Organization) SAR (NISAR) mission, multiple studies with airborne L-band UAVSAR (Uninhabited Aerial Vehicle Synthetic Aperture Radar) data from 2020 NASA SnowEx campaign have already demonstrated the potential of InSAR for snow remote sensing (e.g. Bonnell et al., 2024; Deeb et al., 2021; Hoppinen et al., 2023; Idowu and Marshall, 2022; Marshall et al., 2021; Palomaki and Sproles, 2023; Tarricone et al.,

2022).

InSAR retrieval algorithms need spatial data of snow density and referencing to estimate the spatial variability in absolute snow depth or snow water equivalent (SWE). Leinss et al. (2015) have proposed a modified InSAR technique to circumnavigate the need of snow density in SWE retrievals by introducing an additional parameter with very small variability for a range of incidence angles and snow density, their approach also assumes that the vertical profile of snow density does not change between the two dates for each InSAR pair. However, the density profiles can change depending on the time interval between revisits, new snowfall events, and weather conditions that may impact the top layer of the snowpack. Furthermore, snow density might still be needed in referencing the retrievals to obtain absolute snow depth or SWE for assimilation purposes. Hyper-resolution snow hydrology models driven by realistic hydrometeorological forcing can potentially provide a good estimate ~~of~~ for the InSAR algorithm, and in turn the assimilation of InSAR retrievals can potentially improve the modeled snowpack states. Earlier studies have already shown the potential of assimilating retrieval of snow depth or SWE from airborne or satellite SAR to improve modeled snowpack and reduce uncertainty (e.g. Girotto et al., 2024; Pflug et al., 2024; Shrestha and Barros, 2025).The upcoming launch of the NISAR mission that will provide L-band measurements globally provides impetus to investigate the assimilation of InSAR retrievals and associated uncertainty quantification with potential application to operational water prediction. Here, we leverage the multiple in-situ and airborne snow measurements available from NASA's SnowEx'20 (Marshall et al., 2019) campaign over Grand Mesa to 1) evaluate L-band InSAR retrievals of snow depth, and 2) assimilate the retrievals into a distributed snow hydrology model to evaluate the impact on the simulated macro-physical snow properties and their uncertainties. We evaluate the L-band InSAR retrievals at their native resolution over different snow

depths and land covers against ground-based measurements and airborne Lidar (Light Detection and Ranging) retrievals. While the InSAR retrievals only provide a change in snow depth, data assimilation requires total snow depth. Therefore, we use the airborne lidar measurements of snow depth to reference the InSAR retrievals and obtain the total snow depth. The InSAR retrievals with the common first flight date (but different repeat pass) with airborne lidar measurements of snow depth were used for assimilation at different time windows and the other InSAR retrievals were used to evaluate the ensemble snow hydrology model prediction of snow properties and to characterize the impact of assimilating the InSAR retrievals of snow depth.

2 Methods

2.1 Study Area

The study area is located over the western part of Grand Mesa plateau, Colorado, USA (GM domain; Fig. 1). The land cover is dominated by grassland and mixed forests across the plateau with elevations ranging from 3000 to 3200 m. There are several scattered open water bodies (e.g., lakes and reservoirs), as well as areas with shrubs and wetlands. During the SnowEx'20 campaign, Grand Mesa was used to host an Intensive Observation Period (IOP) during the snow-on season, including bi-weekly UAVSAR flights and airborne Lidar data collections.

2.2 Data

2.2.1 UAVSAR

UAVSAR is a fully polarimetric L-band synthetic aperture radar designed to obtain high quality airborne repeat pass interferometry (Hensley et al., 2008; Rosen et al., 2006). The radar operates at a frequency of 1.26 GHz ($\lambda = 0.2379\ m$) with a bandwidth

of 80 MHz, and is mounted on the NASA NASA Gulfstream III, flying at a nominal altitude of 13800 m. UAVSAR data are available from the ASF-DAAC for multiple campaigns (https://api.daac.asf.alaska.edu/services/utils/mission_list). The uavsar_pytools (Keskinen et al., 2022;https://github.com/SnowEx/uavsar_pytools) was used to download and convert InSAR georeferenced binary grid files to geotiffs in WGS84 for Grand Mesa (SnowEx'20). The interferometric data consists of the interferogram, coherence, unwrapped phase in quad polarizations, including the digital elevation and incidence angles along the flight path. In some cases, all polarizations were not available. There were 7 InSAR pairs available based on 5 UAVSAR flights for repeated flight paths at a heading of 274° (Table 1). The flight maps are available from https://uavsar.jpl.nasa.gov/cgi-bin/data.pl. The interval between the InSAR pairs varied between 7 to 40 days (e.g. track 3-5 (11d), 3-8 (18d), 3-13 (25d),3-17 (40d),5-8 (7d),8-13 (7d) and 13-17 (15d)).

2.2.2 Snow Pit and Snow Pole Measurements

The snow pit data include measurements of snow temperature, snow depth, snow density, snow stratigraphy, snow grain size, liquid water content, and snow water equivalent over Grand Mesa. The SNEX20_GM_SP collection (Vuyovich et al., 2021) has 154 snow pit measurements between 27 January and 12 February 2020. Similarly, the SNEX20_TS_SP collection(Mason et al., 2024) has time-series of snow pit measurements between October 2019 and May 2020, obtained by the SnowEx community during the 2020 campaign.

The snow pole data (SNEX20_SD_TLI**)** consists of snow depth measurements based on time-lapse imagery by capturing a snow pole in each imagery(Breen et al., 2022). The temporal coverage for these data is from 29 September 2019 through 10 June 2020. The cameras took either three images daily (11AM, 12 PM, 1PM) or twice

daily (11AM and 12PM). The cameras were placed in 9 different environments over the Grand Mesa based on tree-density map (treeless, sparse and dense) and snow depth (shallow, intermediate and deep). The snow depth classification was based on Airborne Snow Observatory (ASO) Lidar retrievals from 8 Feb 2017. The error estimates for each camera vary and range from ± 2 to ± 16 cm. More details are also available from https://snow.nasa.gov/sites/default/files/users/user354/SNEX-Campaigns/2020/NASASnowEx20_ExperimentPlan_v15.pdf

2.2.3 ASO

The Airborne Snow Observatory(ASO; Painter et al., 2016) Lidar derived snow depths at 3 m and 50 m resolution for Grand Mesa were available for Feb 1/2 (fused together) and Feb 13 during the SnowEx'20 campaign. The snow depths over forested area represent snow depths at the ground. SWE estimates were also available from ASO at 50 m resolution, based on bias corrected snow density using a snow hydrology model at 50 m resolution. The reported uncertainty in the data was 5.8 cm and 1.7 cm at 3 m resolution for the two dates, and less than 1 cm at 50 m resolution for both dates. In the ASO retrievals for SWE, the snow density was obtained by calibrating the modelled density with ground-based observations.

2.2.4 Atmospheric data

The High-Resolution Rapid Refesh (HRRR;Dowell et al., 2022) 3 km first hour forecast data for water year 2020, was downloaded using a python package(Blaylock, 2024;https://doi.org/10.5281/zenodo.4567540). The HRRR ensemble consists of 36 members for DA and 9 members for forecast run but were not available in the servers except the single forecast. This HRRR data were used both to estimate atmospheric correction of InSAR phase and as offline atmospheric forcing for the snow hydrology model. The HRRR grids interpolated to regular geographic grids are also outlined in

185 the GM domain (Fig. 1).

186 ## 2.3 InSAR snow depth retrieval

187 The total interferometric phase difference obtained with repeat pass SAR data
188 over a snow-covered region includes contributions due to phase impacts from flat
189 Earth, local topography, atmospheric delay, snowpack, and random and systematic
190 errors. While the random error mostly comes from the temporal decorrelation,
191 assuming that phase impacts from flat Earth, local topography and systematic errors
192 are accounted for in the UAVSAR InSAR processing chain, the extraction of the phase
193 contribution only requires accurate estimation of phase contribution due to atmospheric
194 delay (see Appendix A1). With known InSAR phase difference ($\Delta\emptyset_s$) due to the
195 presence of snowpack, the change in snow depth (Δz_s) can be estimated following
196 Guneriussen et al. (2001) for coherent reflections:

197 $$\Delta z_s = -\left(\frac{\lambda}{4\pi}\right)\frac{\Delta\emptyset_s}{\left(cos\theta_i - \sqrt{\varepsilon - sin^2\theta_i}\right)} \quad (1)$$

198 where λ is the SAR wavelength, θ_i is the incidence angle and ε is the bulk
199 snowpack permittivity. For dry snow, ε'' is negligible compared to ε' and the relationship
200 between snow density ρ_s [kgm^{-3}] and permittivity can be expressed according to
201 Matzler, (1996) and Wiesmann and Mätzler (1999) as follows:

202 $$\varepsilon = 1 + 1.6 * 10^{-3}\rho_s + 1.8 * 10^{-9}\rho_s^3 \quad (2)$$

203 Field measurements of density data are generally sparse and may not be
204 available for all the periods. Also, for future NISAR mission, field measurements alone
205 will not be able to provide the snow density for all grid locations. So, we use modeled
206 snow density (MSHM reference run) driven by atmospheric forcing from an operational
207 numerical weather prediction (NWP), which can be applied everywhere to obtain the
208 bulk snowpack permittivity.

Interferometric coherence is important to assess the uncertainty in the retrievals of snow depth, as the retrieval errors increase with decreases in coherence. Ruiz et al. (2022) used a ground based 1-10 GHz SAR system with InSAR capabilities to examine the environmental impact on the observed coherence for snow covered surface. For example, increases in air temperature leading to snow melt are associated with large drops in snow coherence, besides wind, precipitation and large changes in temperature gradients. Compared to X, C and S-band, L-band measurements exhibit higher coherence over longer temporal baselines, and lower error in SWE retrieval, indicating better suitability for InSAR applications.

The estimation of Δz_s following Eq. (1) assumes that the density of the snowpack is uniform with depth and that the underlying profile does not change with time. The latter assumption is problematic as the snow density of the underlying profile could change due to physical processes (e.g. compaction) depending on the temporal baseline of the repeat pass and fresh snow. Besides, natural snowpacks are characterized by multi-layer vertical stratigraphy with varying snow density and the phase delay is an integral of the phase delay over the multiple layers (Liens et al. 2015). Using $\Delta SWE = \sum_{j=1}^{N} \Delta z_{s,j} \rho_s, j/\rho_w$, where ρ_w is the density of water, and i=1,N are the multiple layers, Liens et al. (2015) proposed a linear relationship between InSAR phase change and SWE change as follows:

$$\Delta SWE = -\Delta \emptyset_s \left(\frac{\lambda}{2\pi\alpha}\right)\left(1.59 + \theta_i^{\frac{5}{2}}\right)^{-1} \quad 3$$

where α is an optimal correction factor ranging from $0.92 - 1.07$ for a wide range of incidence angles (up to 65°) and snow densities (up to 900 kgm^{-3}). With this formulation and using an optimal α, they estimated a maximum error of 10%. To reduce the uncertainty in snow density, the above method could be directly used to estimate

changes in SWE. However, errors due to variations in density profile tied to the temporal baseline between the repeat passes remain to be addressed.

Since we evaluate the model results with snow depth measurements from the lidar and ground-based measurements, we employ Eq. 1 for the estimation of snow depth change in this study. Earlier studies (e.g. Bonnell et al., 2024; Marshall et al., 2021; Palomaki and Sproles, 2023) have also used the same approach. Also, InSAR retrievals only provide change in snow depth or SWE, so even for SWE changes, one would require prior SWE measurements or snow depth and snow density to obtain absolute SWE for assimilation. In general, snow depth measurements are more readily available (e.g. lidar or ground measurements) and models with data assimilation can provide close estimate of snow density, so this study also provides a framework for using InSAR snow depth change for data assimilation. Using the atmospherically corrected unwrapped phase images from the UAVSAR data, the snow depth was retrieved over the GM domain in the native grid resolution (approx. 5 m) using average bulk snow density between two repeat pass dates from MSHM reference runs. Note that the estimated change in snow depth is also well below the limit for possible phase wrapping effect in L-band, which is around 69 cm for $\lambda = 23.6\ cm,\ \theta_i = 23°$ and $\rho_s = 300 kg,m^{-3}$. (Deeb et al., 2011).Here, it is also important to note that the estimated change in snow depth is a relative change, and without a snow-free scene or known point change in snow depth, it's not possible to relate the relative change in snow depth to absolute snow depth change. Previous studies (e.g. Bonnell et al., 2024; Conde et al., 2019; Hoppinen et al., 2023; Palomaki and Sproles, 2023; Tarricone et al., 2022) have used different methods (e.g. finding pixels with no changes or using pixels with known changes) to calibrate the InSAR retrievals to obtain absolute change in snow depth or SWE. In this study we use the snow pole measurements over grasslands for the calibration. For cases, where the measurements cannot be collocated due to

missing retrievals, we use the snow pole measurement over the sparsely forested areas. In addition, we use an average over a 3x3 square box in the UAVSAR scene to reduce any uncertainty due to GPS location of snow pole measurements. The InSAR snow depth change for a 3x3 square box (native resolution) was compared with snow pole measurements from treeless environment (W1A, W1B and W3A; linearly interpolated to the time of repeat pass flight) for calibration, and the average value was used for the calibration. For Feb 1-12 retrievals in HV and VH polarization (which had lot of missing data) snow pole measurements from W5A, W6B and W6C were used for calibration. Further, we use VV polarization with higher coherence for spatial evaluation with lidar data, but since it was not available for all retrievals, and HH polarization also exhibit higher coherence and similar results to VV polariztion, HH is used for the InSAR retreivals and data assimilation.

2.4 MPDAF and Experiment Setup

The Multi-Physics Data Assimilation Platform (MPDAFv1.0; Shrestha and Barros, 2025) employs a coupled framework of Multilayer Snow Hydrology Model (MSHMv3.0; Cao and Barros, 2020; Kang and Barros, 2011b, 2011a; Shrestha and Barros, 2025) and the NCAR Data Assimilation Research Testbed (DART; Anderson et al., 2009; DART, 2023). MSHM is a distributed 1D-column model, that solves the mass and energy budgets of the snowpack. Key physical processes of snow hydrology - snow/rain partitioning, snow accumulation, compaction, melting, melt-runoff including snow microstructure evolution are well represented in the model to simulate the macroscopic and microscopic snow properties. The snow microstructure evolution is simulated using a detailed microphysical scheme based on the CROCUS snowpack model (Vionnet et al., 2012). The bottom boundary conditions are kept constant during

the cold season assuming frozen soils for snow-on conditions and fixed deep soil temperature. Fresh snow density in this study is based on the parameterization of Hedstrom and Pomeroy (1998) and wet bulb temperature is used as threshold to partition precipitation as rain or snow (Wang et al., 2019). Currently, the rain versus snow partitioning only allows for existence of rain or snow and does not allow for mixed form of rain/snow. More details about the parameterizations can be inferred from the studies mentioned above. Following Cao & Barros (2020), the snow albedo is provided externally using the NLDAS Mosaic Land Surface Model L4 v2.0 albedo data (Xia et al., 2012a; Xia et al., 2012b).

In DART, we use the Ensemble Adjustment Kalman Filter (EAKF;Anderson, 2003) with enhanced spatially varying state space inflation (Anderson, 2009; El Gharamti, 2018). Assimilation is carried out with observed integrated quantities like total SWE or total snow depth, and the increments are then distributed vertically to the model states (snow depth, snow density and SWE) using a repartition algorithm (Shrestha and Barros, 2025)(Shrestha & Barros, 2024).

For ensemble Kalman filters, ensemble size fewer than 20-30 can lead to statistical error and larger ensemble size take longer to run with very little benefit. So, 30-100 ensemble size is recommended to use with ensemble Kalman filters in DART. In this study, we have only two DART state vectors and use 48 ensemble members which is also constrained by the computational and data storage requirements for hyper-resolution runs. In MSHM, vertically discretized snow depth and SWE are prognostic variables. However, we only use the integrated quantities of these prognostic variables (i.e. total SWE and total snow depth) as state vectors in DART, which are updated by the ensemble filters (e.g. EAKF used here). The ensemble filter assumes a Gaussian relation between the variables in the joint state space prior distribution. First, update increments are computed for each ensemble sample of the

observation variable, which is then used to solve for the increments for each state variable. This requires prior cross covariance of each state variable with observation variable along with variance of the observation variable (see Anderson 2003 for details). Then, we use a newly developed repartition algorithm to distribute the increments in the vertical profile with mass conservation (snow density is updated). For bulk or single layer snow hydrology models, such repartitioning is not needed. DA directly impacts the top layers of the snowpack where snow is added or removed based on assimilation increments. The lower layers are only impacted by the modeled snow evolution after the assimilation, primarily due to addition of new layers on top or removal of existing snow layers. The localization setups were used such that the observations only impact model grid points where they are located. The goal is to reduce the impact to surrounding grids with different landcover characteristics, and therefore different retrieval uncertainty such as in the case of forested and non-forested grid points. So, the cutoff radius that determines the region of spatial impact of the assimilated variable was set at approximately 100 m (close to the model resolution).

The snow hydrology model is setup over the GM domain using approximately 90 m resolution with 66×165 grid points. The maximum number of snow layers in the model was set to 30. The merged atmospheric forcing data are also interpolated to regular geographic grid and disaggregated to 90 m resolution. Here, no downscaling algorithms are applied to the forcing data and the disaggregation technique applies homogeneous forcing over the subgrid pixels – this also allows us to highlight the impact of hyper-resolution data assimilation. Further, scaling analysis of SAR backscatter and Lidar snow depth estimates in mountainous regions including Grand Mesa (Manickam and Barros, 2020; Mendoza et al., 2020b, a) shows that minimum variance is reached at scales 100-250 m with clear scaling breaks tied to very high variance at very small scales and topography and land-cover at larger scales. The

spatial resolution of this study is around the scale of minimum variance.

The MSHM reference run (CTRL) was integrated from Oct 1, 2019, to Apr 1, 2020 using the default HRRR forcing data. For data assimilation (DA) runs, 48 ensemble members were generated by perturbing the model forcing data. The precipitation is perturbed using multiplicative noise drawn from a uniform distribution U[−0.4, 0.4]. The incoming shortwave and longwave are also perturbed using a multiplicative noise from a uniform distribution U[−0.05, 0.05] and U[−0.1, 0.1] respectively.

Figure 2 synthesizes the availability of ASO Lidar retrievals and L-band InSAR retrievals for assimilation and evaluation of model runs. Here, we use part of the data for assimilation and the remainder are used for evaluation. As stated earlier, the L-band InSAR retrievals only provide information about relative changes in snow depth or SWE, which need to be referenced and calibrated to obtain absolute values needed for assimilation. In the context of distributed modelling at a given resolution, this would require a spatial map of snow depth or SWE for referencing. In this study, we use the ASO Lidar snow depth data at 50 m resolution (Feb 1) as a reference. We aggregate the InSAR retrievals to coarser resolution (50 m) to match with the resolution of the reference ASO Lidar snow depth retrieval. and Then, we combine the reference snow depth withem with aggregated InSAR retrievals of snow depth change I1 (Feb 1-12) , I2 (Feb 1-19) and I3 (Feb 1-26) at 50 m resolution to obtain the absolute snow depth pattern over the GM domain on Feb 12, 19 and 26 respectively. Two data assimilationDA experiments are conducted by assimilating total snow depth: 1) ASO Lidar retrieval on Feb 1 (DA), and 2) ASO Lidar retrieval on Feb 1 and referenced InSAR retrievals on Feb 12,19 and 26 (DAU). We reference the InSAR retrievals by aggregating the data to 50 m resolution grid of the ASO Lidar retrievals from Feb 1, which matches the date of the first InSAR pair in both cases. InSAR retrievals of snow depth change on I5 (Feb 12-19), I6 (Feb 19-26) and I7 (Feb 26-Mar12) are reserved

for independent evaluation. In both DA experiments, we assign an observational error of 10 % for the snow depth retrievals at 50 m resolution, that is consistent with the errors from the InSAR retrievals using the UAVSAR data in this study.

3 Results

3.1 Meteorological Settings

The meteorological conditions based on the HRRR forcing data including air temperature, precipitation and wind speed were analysed for the GM domain (2*5 HRRR grids at 3 km resolution). These environmental forcings along with temporal baselines are also the source of variability in interferometric coherence and errors in the retrievals. Figure 3 shows the time-series of air temperature, wind speed and precipitation intensity for the month of February including the first two weeks in March for the NW corner of the GM domain. The month of February was generally cold and windy with temperatures dropping below -20 °C, and wind speeds reaching up to 15 m/s. The time-series show cooling and warming periods at a weekly time scale, with some days where the air temperature reached above zero. However, the amplitude of cooling decreases gradually from the end of February to mid-March with more frequent warm periods. There were a few snowfall events between Feb 1-12, Feb 19-26 and Feb 26-Mar 12, which varied in intensity along the GM domain.

3.2 Snow Density

A spatial pattern of bulk snow density is required to compute the snowpack permittivity needed for the InSAR retrieval technique. Uncertainty in snow density estimates can lead to errors in snow depth retrieval. Figure 4 shows the snow density distribution for the InSAR pair (Feb 1-12) using the 50 m resolution ASO Lidar data,

386 snow pit data and model estimates using a reference run (CTRL) for the GM domain.
387 Only the snow pit data within GM domain collected within ± 1 day of the InSAR flights
388 were used for analysis. All three data sets show compaction of snow between the two
389 dates, but the model simulates slightly higher snow density for both flight dates and
390 underestimates the spatial variance as observed in the snow pit data and ASO Lidar
391 data as expected given the coarse resolution of the HRRR precipitation forcing (i.e.
392 3km). Note that the snow density in ASO Lidar data is also from a model estimate but
393 it was bias corrected (i.e., locally calibrated) using the snow pit data from SnowEX'20
394 campaign. In the 11-day temporal baseline, the average snow density changes by
395 5.6 %, 11 % and 4 % respectively among the lidar, snow pit and model data. Here, we
396 have to note that the snow density change in pit data could also be attributed due to
397 spatial variability besides compaction, which could be contributing to higher
398 differences.

399 To examine the error in snow depth retrieval associated with error in density, we
400 used Eq. 1 to retrieve snow depth change for a fixed phase change due to snow. Figure
401 4d shows the variability in InSAR retrieval of snow depth change as a function of
402 incidence angle, for a phase change of -0.17π using the average snow density from
403 ASO Lidar, snow pit and the MSHM CTRL run. The error generally decreases with
404 increasing incidence angle. The synthetic simulation shows that a 10 % error in snow
405 density can lead to approximately 10 % error in snow depth estimates at lower
406 incidence angles, everything else being the same.

407 3.3 L-band retrieval of snow depth

408 The temporal baselines for the L-band retrieval range from 7 to 40 days, and the
409 interferometric coherence generally decreased with increasing temporal base lines as
410 expected. For treeless and forested areas, the mean coherence for 7-day temporal

411 baseline (Feb 12-19) was 0.7 ± 0.15 and 0.65 ± 0.18 respectively. Similarly, for the Feb
412 19-26 pair, it was 0.6 ± 0.18 to and 0.5 ± 0.2 respectively. The coherence decreased to
413 0.39 ± 0.16 and 0.36 ± 0.17 for the 40-day temporal baseline. These values are for the
414 HH polarization, as it was available for all dates (see Table 2). The lower coherence
415 for the Feb 19-26 pair compared to Feb 12-19 pair could be attributed to environmental
416 factors, e.g., larger wind speeds, precipitation event, and intermittent warming (see
417 Fig. 3). The forested area exhibits lower coherence than the treeless area suggesting
418 possible higher uncertainty in the retrievals. The above statistics are based on the
419 NLCD landcover data at 30 m resolution, whereas the native resolution of InSAR
420 retrievals from UAVSAR is in the order of 5 m resolution, and the retrievals over forest
421 contain information from snow depth in tree clearings as well.

422 **3.3.1 Evaluation with ASO Lidar data**

423 The InSAR pair of Feb 1-12 with a temporal baseline of 11 days provides the
424 closest concurrent pair with the ASO Lidar retrieval based on Feb1/2 and Feb 13 to
425 compare the snow depth difference at a scale of 3-5 m resolution. Figures 5a-b show
426 the spatial pattern of interferometric coherence and snow depth change at VV
427 polarization. Figure 5c shows the change in snow depth based on ASO Lidar data for
428 the same region. The western part of this GM subdomain is mostly dominated by snow
429 cover over grasslands, while the eastern part contains snow cover in forested areas
430 with relatively lower coherence. Both the Lidar and L-band retrieval capture the wavy
431 roll like pattern due to scouring and drifting of snow over the grasslands shown earlier
432 by Marshall et al. (2021) for a smaller area. Over the eastern part of the subdomain,
433 which is dominated by forest, there are significant discrepancies: in regions with no
434 snow depth change in the ASO Lidar data, a decrease in snow depth is observed in
435 the L-band retrieval.

436 The average coherence values for this subdomain were 0.51, 0.46, 0.39 and 0.39
437 for VV, HH, HV and VH polarization respectively. Also, the missing retrievals in the
438 radar scene were 8, 11, 36 and 54 % of the area respectively for the different
439 polarizations (see Table 3). The distribution of snow depth change for co-polarization
440 better matches with the ASO Lidar data compared to cross-polarization (Fig. 5d). The
441 average changes in snow depth for the scene were -2.42, -1.13 and -0.1 cm
442 respectively for ASO Lidar and InSAR VV and HH polarizations. The HV and VH
443 polarization show rightward and leftward shifted peaks respectively. The impact of
444 atmospheric correction was minimal for this retrieval. With and without atmospheric
445 correction, the average snow depth change for the InSAR retrieval (VV) were -1.28 cm
446 and -1.13 cm respectively for the scene. The ASO Lidar and InSAR retrieval are in
447 similar resolution but differ in geolocations, so a quantitative spatial comparison which
448 would require spatial interpolation was not used, but we only explore the patterns and
449 frequency distributions within the same extent. For the frequency distribution (Fig. 5d)
450 between ASO and InSAR (VV), we find R=0.97 and RMSE=2.03 cm, and the previous
451 study (Marshall et al. 2021) found R=0.76, RMSE=4.7cm using the near surface field
452 measured density observations in the retrieval.
453 While the results were similar for other subdomains (not presented here), the L-
454 band retrievals were found to show a general decrease in snow depth in the western
455 most part of GM domain dominated by forest cover, while the Lidar data shows a
456 contrasting increase in snow depth. Thus, the retrievals show higher uncertainty over
457 the forest areas and further evaluation is needed.

458 **3.3.2 Evaluation with snow pole and snow pit time-series data**

459 The snow pole data provide a time-series of snow depth measurements for
460 locations which are treeless or have sparse/dense trees and can be used for

461 comparison with all available InSAR pairs over the GM domain. We use the linearly
462 interpolated snow pole data in time to reference the InSAR retrievals in HH polarization
463 and obtain absolute snow depth for comparison. Figure 6 shows the evaluation of
464 referenced InSAR retrievals with snow pole data for treeless landcover: a-c), sparse
465 trees : d-f), and dense trees : g-m). In most cases, the L-band InSAR retrievals capture
466 the trend in snow depth change very well for different landcover types. The root mean
467 square errors (RMSE) were similar for different landcovers with approximate values of
468 4-6 cm (which is consistent with earlier findings by Marshall et al. (2021) for same
469 InSAR retrieval but different data for evaluation). We also explored the errors in terms
470 of InSAR pairs. The RMSEs of InSAR estimates were 5.0, 4.9, 4.4, 6.2, 7.3 and 4.2 cm
471 respectively for Feb 1-12 (11d), Feb 1-19(18d), Feb 1-26(25d), Feb 12-19(7d), Feb 19-
472 26(7d) and Feb 26-Mar 12(18d) retrievals at the 12 stations. The errors in InSAR
473 retrievals are within 4-8 % of the absolute snow depth.

474 The time-series from snow pits in the north-western part of the GM domain also
475 provide valuable snow depth measurements to evaluate the InSAR estimates. The
476 time-series contains data across treeless and forest areas (Fig. 7). Here, again we use
477 the snow pit measurements to reference the InSAR retrievals and obtain the absolute
478 snow depth. It must be noted that snow pit measurements were carried out at different
479 locations, but within a few meters. Here, we must note that the temporal variability in
480 the snow depth is also partly contributed by the spatial variability due to change in
481 location of pits. The snow depth was slightly higher for the treeless area compared to
482 the forested area, which were within 0.25 km of each other. The InSAR retrievals can
483 capture some of the trends very well, while showing contrasting results for others like
484 for the case of the snow poles. The coherence was within 0.12-0.67 and 0.33-0.79 for
485 the treeless and forested areas, respectively. The errors were 2-9 % and 3-31%
486 respectively for treeless and forest areas. Based on the two comparisons of InSAR

retrievals against snow pole and snow pit data, the errors are within 10 % for most of the retrievals with few exceptions.

3.4 Data Assimilation and Evaluation

In this section, we explore the impact of assimilating L-band InSAR retrievals on modeled SWE and particularly modeled snow depth. As already discussed in Section 2.4, we use two assimilation experiments including an open loop (without assimilation) and a reference run to explore the time evolution of modeled snowpack over Grand Mesa for the accumulation season in the water year 2020. Figure 8 shows the time-series of spatially averaged modeled snow depth from the different runs. The spatial averaging was done for the grids without trees and open water over the GM domain. The dotted lines indicate the total spread of the ensemble runs. The assimilation of the ASO lidar snow depth on Feb 1 shifts the ensembles upwards and reduces the spread for both DA and DAU runs. It shows that the reference run (CTRL) was largely underestimating snow depth. While some of the ensemble members with positive perturbation of precipitation of precipitation were able to capture the actual snow depth, the ensembles with negative perturbation of precipitation underestimated the total snow depth (see the spread in OL run). The assimilation of referenced InSAR retrievals for Feb 12, 19 and 26 (DAU runs) exhibit a small increase in snow depth for the ensemble averages compared to DA runs.

The modeled snowpack was also compared with in-situ measurements to assess the impact of data assimilation. The modeled snow depth and SWE at 90 m resolution were compared to snow pit data (IOP and TSD) in locations without trees. The land cover filtered IOP data contained snow depth and SWE from 28 Jan 2020 to 12 Feb 2020. Similarly, the land cover filtered TSD contained snow depth from 19 Dec 2019 to Apr 17, 2020. There were 68 IOP and 12 TSD snow pit data available for comparison

512 across the GM domain based on the model simulation spatial extent. The RMSE
513 decreased from 35.2 cm to 18.3 cm for snow depth, and for SWE it decreased from
514 8.9 cm to 5.9 cm. The differences in RMSE between DA and DAU runs for these pits
515 were negligible. The modeled snow depth was also compared against snow pole
516 measurements for locations without trees (3 locations, W1A, W1B and W3A) for the
517 entire model simulation period. The RMSE were 17.6, 21.2 and 27.2 cm for the CTRL
518 run, and decreased to 8.1, 21, and 20.8 cm for the DA runs. For DAU runs, the rmse
519 were 8.5, 22.2 and 19.2 cm respectively (see Table 4).

520 The spatial pattern of the modeled snow depth can be evaluated using the
521 reserved InSAR retrievals from Feb 12-19, Feb 19-26 and Feb 26-Mar12 pairs, that
522 were not used for assimilation. Figure 9 shows the spatial pattern of snow depth
523 change for these repeat pass retrieval dates along with their distribution for the entire
524 GM domain. The estimates are shown for the retrievals and all the model runs. The
525 InSAR data were aggregated to 90 m resolution for comparison. And the grids with
526 open water bodies and tree covers (sparse or dense) were all masked out. Additionally,
527 for the ensemble runs, the spatial maps were obtained by averaging the ensembles,
528 and the distributions are for the averaged ensembles.

529 The InSAR retrievals for Feb 12-19 and Feb 19-26 exhibit both increase and
530 decreases in snow depth for the GM domain, while the retrievals for Feb 26-Mar 12
531 show increase in snow depth only (Fig. 9a-c). As expected, the ensemble average for
532 the open loop (OL) run shows spatial variability at the scale of the atmospheric forcing.
533 The OL run shows similar tendency as InSAR retrievals, except for Feb 12-19 pair,
534 where it shows decrease in snow depth (Fig. 9d-f). While the DA runs improve the total
535 snow depth and SWE, no improvement in the snow depth change is achieved for the
536 Feb 12-19 pair (Fig. 9g). In addition, there are more grids with decrease in snow depth
537 for the remaining two pairs (Fig. 9h-i) compared to the OL run. Note that the DA does

increase the modeled spatial variability in snow depth change.

Compared to other model runs, DAU produces best results with positive increase in snow depth change (Fig. 9j-k), also seen in the widening of the distribution in the positive direction (Fig. 9m-n). This is due to the assimilation of InSAR data on Feb 19 and 26. Since there was no assimilation of InSAR data on Mar 12, there is no improvement in the modeled snow depth change for Feb 26-Mar 12 even in DAU runs (Fig. 9i and Fig. 9l). The increase or relatively larger increase in snow depth change for DAU runs (Fig. 9j-l) are mostly for the grids where the InSAR data were available for assimilation (Feb 19 and Feb 26). However, the impact of this assimilation appears local in time, and it does produce any significant improvement for the Feb 26-Mar 12 pair compared to DA runs. Despite the data constraints, these results indicate that the assimilation of InSAR estimates has the potential to improve the spatial pattern of modeled snow depth change. Because the snow depth evolution is accumulative, these changes will impact the overall seasonal evolution of the snowpack.

4 Discussion

The hyper-resolution InSAR retrievals resolve the wavy roll like patterns due to scouring and drifting of snow over the grasslands as captured by the ASO lidar data over the grasslands in the NW part of GM domain, also shown earlier by Marshall et al. (2021). However, over forested regions, there are disagreements between the lidar and the InSAR estimates with possible uncertainty in both data sets. The average coherence was similar for VV and HH polarization with slightly higher values for VV polarization and lower for HV and VH polarizations. This resulted in higher percentage of missing retrievals in cross-polarizations. The scene-wide average coherence in HH polarization for the 7-day temporal baseline (treeless area) in the GM domain is around

562 0.6-0.7 which is consistent with values reported by Ruiz et al. (2022). Similarly, the
563 coherence was around 0.5-0.65 for the forested area indicating that the L-band can
564 maintain good coherence over canopy and, with sufficient penetration depending on
565 tree density and canopy architecture, it can be useful in measuring ground snow depth
566 changes. The forested areas generally exhibited lower coherence as expected and the
567 coherence differences between treeless and forested areas were around 14-23% to
568 8 % for 7-day and 40-day temporal baselines, respectively. Overall, the InSAR
569 retrievals generally compare well with in-situ measurements from snow pole and snow
570 pit over sparse and dense forests. RMSE of the lidar measurements over snow pole
571 site used in the study was also around 7-8 cm for the two dates exhibiting good
572 accuracy. So, more data is required for spatial comparison in forested environments to
573 better understand the differences between lidar and InSAR retrievals.

574 The interferometric coherence across the GM domain generally decreased with
575 increasing temporal baseline (e.g. by 44 % from 7 to 40-day temporal baseline). This
576 indicates that the retrieval uncertainty and retrieval error will increase with larger time
577 between the repeat passes as expected. Since the underlying density of snowpack will
578 also change between the repeat passes, the retrieval error will also increase when
579 using a constant density in Eq. 1. In this study, the depth weighted density averages
580 or the average bulk density between two repeat pass dates from the reference MSHM
581 model runs were used for the InSAR retrievals. The reference runs generally
582 underestimated the total snow depth and SWE compared to the ASO lidar data and
583 snow pit measurements, but the bulk snow density was slightly higher than the snow
584 pit observations during the IOP over Grand Mesa. This indicates that the HRRR forcing
585 used for the study underestimates the snowfall events, besides model uncertainty
586 associated with wind redistribution of snow which is not accounted for. The modelled
587 higher bulk density could again indicate uncertainty in the fresh snow density(Cao and

588 Barros, 2020; Shrestha and Barros, 2025) and compaction parameterization (e.g.
589 Abolafia-Rosenzweig et al., 2024). The modelled layered snowpack generally shows
590 a two-layer density profile, with an upper layer exhibiting a gradient and near constant
591 density profile in the lower layer. Upon examining density profiles, the difference in
592 snow density profile in the lower layer varied between 1.5-1.8 % (Feb 19-26) and 6-
593 7 % (Feb 1-26) for 7-day and 25-day temporal baseline. This could be still a lower
594 estimate than the actual change in snow density, as shown earlier for 11-day temporal
595 baseline, which was 4 and 11 % for model and snow pit observations. Therefore, the
596 variability in snow density profiles is small for the 7-day base line, and it is large for 25-
597 day base line during the accumulation period. Besides the modelled density has its
598 own bias compared to actual snowpack density due to forcing and model structural
599 uncertainty. However, the calibration of the retrievals to obtain absolute snow depth
600 change from the relative snow depth change could also compensate for these errors.
601 Further in-depth studies are needed to better understand the sources of error.
602 Data assimilation of the ASO Lidar snow depth reduces the error and uncertainty
603 in the modeled snow depth. This also reduced the bulk snow density for the ensemble
604 members with lower snow depth (compared to CTRL run) by 4-5 %, as new snow with
605 lower density is added on the top by the repartition algorithm (Shrestha and Barros,
606 2025). These ensemble members (DA; Fig. 9h-i) also exhibited lower or negative snow
607 depth change for Feb 19-26 and Feb 26-Mar 12 compared to OL ensembles, which is
608 reflected in the ensemble averages over the GM domain. However, the assimilation of
609 referenced InSAR retrievals (DAU) produces increase in snow depth changes in the
610 ensemble average compared to DA runs. The impact is most apparent in the grids of
611 the GM domain where the data were available for assimilation. This produced the best
612 distribution of snow depth change compared to observations, showing the potential of
613 InSAR retrievals in improving the modeled snowpack. It also demonstrates HRRR

underestimation of snowfall between the dates of the InSAR pairs (e.g. between Feb 26 and Mar 12) and it explains the small snow depth differences in the OL runs compared to InSAR retrievals. The OL shows the increase in snow depth due to snowfall just before Mar 12 (see Fig. 3) albeit underestimated as indicated by the difference in magnitude between the InSAR retrievals and the OL snow depth changes. Likewise, the impact of assimilating InSAR retrievals which improves the simulated snow depth changes (as seen for the first two pairs) highlights the need for high temporal resolution of SAR measurements.

5 Conclusion

This study shows that InSAR retrievals are useful to improve the snowpack simulation and capture its spatial and temporal variability. The assimilation of hyper-resolution retrievals of snow depth is equivalent to a downscaling of precipitation forcing with a bias correction besides additional contribution from physical processes not resolved by the model at the given scale. The RMSE of the InSAR retrievals of absolute snow depth change at native resolution compared to snow pole measurements over different land covers were within 4-6 cm, which corresponds to less than 10 % of the absolute snow depth. However, reference snow depth or SWE is essential to obtain absolute snow depth or SWE for assimilation purposes, which poses a challenge in an operational context. In this situation, one would start from snow-free conditions and build up the absolute snow depth from InSAR retrievals using the prior estimates as reference. Accurate calibration of the estimated relative snow depth change, or SWE will be important to minimize retrieval errors. Further work is also essential for InSAR retrievals in forested areas and complex terrains. Future studies are needed to advance a general framework for calibrating InSAR retrievals and

638 obtaining absolute snow depth or SWE for assimilation into the models.

639

Code availability

The MPDAF software with experiment setups is available from https://github.com/APBarrosResearchGroupopen/mpdaf.git. MSHM v3.0 used here is documented in ~~The MPDAF v1.0 software with experiment setups is available from https://github.com/mpdaf23/mpdaf.git. MSHM v3.0 used here is documented in (~~Cao and Barros (~~,~~ 2020); Kang and Barros (~~,~~ 2011b, a); Shrestha and Barros (~~,~~ 2025)~~)Kang and Barros (2011a, 2011b); Cao and Barros (2020) including the updates described in this paper~~. MEMLS is documented in Proksch et al., (2015~~))~~ and can be obtained with email to the respective authors. ~~MEMLS can be downloaded from http://www.iapmw.unibe.ch/research/projects/snowtools/memls.html.~~ The NCAR DART can be downloaded from https://github.com/NCAR/DART.git.

Data availability

The NASA SnowEx 2020 observation data can be downloaded from NASA National Snow and Ice Data Center Distributed Active Archive Center and ASF DAAC. HRRR atmospheric forcing data can be now downloaded from Amazon Web Services (AWS) courtesy of National Oceanic and Atmospheric Administration (NOAA) and the Registry of Open Data on AWS. The NLDAS albedo data can be downloaded from the NASA GES DISC. Model data and software used for visualization is available from https://uofi.box.com/v/InSARmodeldata.

Author contribution

PS and APB conceptualized the study. PS designed the study, processed the data, conducted the model simulation with data assimilation, carried out the analysis, and wrote the paper. APB acquired the grant for the study and contributed to editing of the manuscript.

Competing interests

The authors declare that they have no conflict of interest.

Acknowledgements

The funding for this study was provided by the National Oceanic and Atmospheric Administration (NOAA), awarded to the Cooperative Institute for Research on Hydrology (CIROH) through the NOAA Cooperative Agreement with The University of Alabama, NA22NWS4320003. This study made use of the Illinois Campus Cluster, a computing resource that is operated by the Illinois Campus Cluster Program (ICCP) in conjunction with the National Center for Supercomputing Applications (NCSA) and which is supported by funds from the University of Illinois at Urbana-Champaign. The analysis of data was done using the NCAR Command Language (Version 6.6.2). We would like to particularly acknowledge the NASA SnowEx campaign including the field and airborne crews who collected the data used in this study. We also acknowledge the collaboration in SnowEx Hackweek which led to the development of multiple tools for downloading and processing data used in this study. The data used in this effort were acquired as part of the activities of NASA's Science Mission Directorate and are archived and distributed by the Goddard Earth Sciences (GES) Data and Information Services Center (DISC).

References

Abolafia-Rosenzweig, R., He, C., Chen, F., and Barlage, M.: Evaluating and enhancing snow compaction process in the Noah-MP land surface model, J Adv Model Earth Syst, 16, e2023MS003869, 2024.

Anderson, J.: Spatially and temporally varying adaptive covariance inflation for ensemble filters, Tellus A: Dynamic meteorology and oceanography, 61, 72–83, 2009.

Anderson, J., Hoar, T., Raeder, K., Liu, H., Collins, N., Torn, R., and Avellano, A.: The data assimilation research testbed: A community facility, Bull Am Meteorol Soc, 90, 1283–1296, 2009.

Anderson, J. L.: A local least squares framework for ensemble filtering, Mon Weather Rev, 131, 634–642, 2003.

Blaylock, B. K.: Herbie: Retrieve Numerical Weather Prediction Model Data, https://doi.org/10.5281/zenodo.13329302, August 2024.

Bonnell, R., McGrath, D., Tarricone, J., Marshall, H.-P., Bump, E., Duncan, C., Kampf, S., Lou, Y., Olsen-Mikitowicz, A., and Sears, M.: Evaluating L-band InSAR Snow Water Equivalent Retrievals with Repeat Ground-Penetrating Radar and Terrestrial Lidar Surveys in Northern Colorado, EGUsphere, 2024, 1–33, 2024.

Breen, C. M., Hiemstra, C., Vuyovich, C. M., and Mason, M.: SnowEx20 Grand Mesa Snow Depth from Snow Pole Time-Lapse Imagery, Version 1, Boulder, Colorado USA, 2022.

Cao, Y. and Barros, A. P.: Weather-dependent nonlinear microwave behavior of seasonal high-elevation snowpacks, Remote Sens (Basel), 12, 3422, 2020.

Conde, V., Nico, G., Mateus, P., Catalão, J., Kontu, A., and Gritsevich, M.: On the estimation of temporal changes of snow water equivalent by spaceborne SAR interferometry: a new application for the Sentinel-1 mission, Journal of Hydrology and

715 Hydromechanics, 67, 93–100, 2019.
716 Dagurov, P. N., Chimitdorzhiev, T. N., Dmitriev, A. V, and Dobrynin, S. I.:
717 Estimation of snow water equivalent from L-band radar interferometry: simulation and
718 experiment, Int J Remote Sens, 41, 9328–9359, 2020.
719 DART: The data assimilation research testbed (version 10.7.3), Boulder,
720 Coloardo, 2023.
721 Deeb, E., Forster, R., Vuyovich, C., Elder, K., Hiemstra, C., and Lund, J.: L-band
722 InSAR depth retrieval during the NASA SnowEx 2020 campaign: Grand mesa,
723 Colorado, in: 2021 IEEE International Geoscience and Remote Sensing Symposium
724 IGARSS, 625–627, 2021.
725 Deeb, E. J., Forster, R. R., and Kane, D. L.: Monitoring snowpack evolution using
726 interferometric synthetic aperture radar on the North Slope of Alaska, USA, Int J
727 Remote Sens, 32, 3985–4003, 2011.
728 Dowell, D. C., Alexander, C. R., James, E. P., Weygandt, S. S., Benjamin, S. G.,
729 Manikin, G. S., Blake, B. T., Brown, J. M., Olson, J. B., and Hu, M.: The High-Resolution
730 Rapid Refresh (HRRR): An hourly updating convection-allowing forecast model. Part
731 I: Motivation and system description, Weather Forecast, 37, 1371–1395, 2022.
732 El Gharamti, M.: Enhanced adaptive inflation algorithm for ensemble filters, Mon
733 Weather Rev, 146, 623–640, 2018.
734 Girotto, M., Formetta, G., Azimi, S., Bachand, C., Cowherd, M., De Lannoy, G.,
735 Lievens, H., Modanesi, S., Raleigh, M. S., and Rigon, R.: Identifying snowfall elevation
736 patterns by assimilating satellite-based snow depth retrievals, Science of The Total
737 Environment, 906, 167312, 2024.
738 Guneriussen, T., Hogda, K. A., Johnsen, H., and Lauknes, I.: InSAR for estimation
739 of changes in snow water equivalent of dry snow, IEEE Transactions on Geoscience
740 and Remote Sensing, 39, 2101–2108, 2001.

741 Hanssen, R. F.: Radar interferometry: data interpretation and error analysis,
742 Springer Science & Business Media, 2001.
743 Hensley, S., Wheeler, K., Sadowy, G., Jones, C., Shaffer, S., Zebker, H., Miller,
744 T., Heavey, B., Chuang, E., and Chao, R.: The UAVSAR instrument: Description and
745 first results, in: 2008 IEEE Radar Conference, 1–6, 2008.
746 Hoppinen, Z. M., Oveisgharan, S., Marshall, H.-P., Mower, R., Elder, K., and
747 Vuyovich, C.: Snow Water Equivalent Retrieval Over Idaho, Part B: Using L-band
748 UAVSAR Repeat-Pass Interferometry, The Cryosphere Discussions, 2023, 1–24,
749 2023.
750 Idowu, A. N. and Marshall, H.-P.: Snow depth retrieval from L-band data based
751 on repeat pass InSAR techniques, in: IGARSS 2022-2022 IEEE International
752 Geoscience and Remote Sensing Symposium, 4248–4251, 2022.
753 Kang, D. H. and Barros, A. P.: Observing system simulation of snow microwave
754 emissions over data sparse regions—Part I: Single layer physics, IEEE transactions
755 on geoscience and remote sensing, 50, 1785–1805, 2011a.
756 Kang, D. H. and Barros, A. P.: Observing system simulation of snow microwave
757 emissions over data sparse regions—Part II: Multilayer physics, IEEE transactions on
758 geoscience and remote sensing, 50, 1806–1820, 2011b.
759 Keskinen, Z., Tarricone, J., Surfix, and Marshall, H.: SnowEx/uavsar_pytools:
760 v0.2.0, https://doi.org/10.5281/zenodo.6578193, May 2022.
761 Lei, Y., Shi, J., Liang, C., Werner, C., and Siqueira, P.: Snow Water Equivalent
762 Retrieval Using Spaceborne Repeat-Pass L-Band SAR Interferometry Over Sparse
763 Vegetation Covered Regions, in: IGARSS 2023-2023 IEEE International Geoscience
764 and Remote Sensing Symposium, 852–855, 2023.
765 Leinss, S., Wiesmann, A., Lemmetyinen, J., and Hajnsek, I.: Snow water
766 equivalent of dry snow measured by differential interferometry, IEEE J Sel Top Appl

767 Earth Obs Remote Sens, 8, 3773–3790, 2015.
768 Li, H., Xiao, P., Feng, X., He, G., and Wang, Z.: Monitoring snow depth and its
769 change using repeat-pass interferometric SAR in Manas River Basin, in: 2016 IEEE
770 International Geoscience and Remote Sensing Symposium (IGARSS), 4936–4939,
771 2016.
772 Li, S. and Sturm, M.: Patterns of wind-drifted snow on the Alaskan arctic slope,
773 detected with ERS-1 interferometric SAR, Journal of Glaciology, 48, 495–504, 2002.
774 Lievens, H., Demuzere, M., Marshall, H.-P., Reichle, R. H., Brucker, L., Brangers,
775 I., de Rosnay, P., Dumont, M., Girotto, M., and Immerzeel, W. W.: Snow depth variability
776 in the Northern Hemisphere mountains observed from space, Nat Commun, 10, 4629,
777 2019.
778 Lievens, H., Brangers, I., Marshall, H.-P., Jonas, T., Olefs, M., and De Lannoy,
779 G.: Sentinel-1 snow depth retrieval at sub-kilometer resolution over the European Alps,
780 Cryosphere, 16, 159–177, 2022.
781 Liu, Y., Li, L., Yang, J., Chen, X., and Hao, J.: Estimating snow depth using multi-
782 source data fusion based on the D-InSAR method and 3DVAR fusion algorithm,
783 Remote Sens (Basel), 9, 1195, 2017.
784 Manickam, S. and Barros, A.: Parsing synthetic aperture radar measurements of
785 snow in complex terrain: Scaling behaviour and sensitivity to snow wetness and
786 landcover, Remote Sens (Basel), 12, 483, 2020.
787 Marshall, H. , V. C. , H. C. , B. L. , E. K. , D. J. , and N. J.: NASA SnowEx 2020
788 Experiment Plan, 2019.
789 Marshall, H.-P., Deeb, E., Forster, R., Vuyovich, C., Elder, K., Hiemstra, C., and
790 Lund, J.: L-band InSAR depth retrieval during the NASA SnowEx 2020 campaign:
791 Grand mesa, Colorado, in: 2021 IEEE International Geoscience and Remote Sensing
792 Symposium IGARSS, 625–627, 2021.

793 Mason, M., Marshall, H., McCormick, M., Craaybeek, D., Elder, K., and Vuyovich,
794 C. M.: SnowEx20 Time Series Snow Pit Measurements, Version 2, Boulder, Colorado
795 USA, 2024.
796 Matzler, C.: Microwave permittivity of dry snow, IEEE Transactions on
797 Geoscience and Remote Sensing, 34, 573–581, 1996.
798 Mendoza, P. A., Musselman, K. N., Revuelto, J., Deems, J. S., López-Moreno, J.
799 I., and McPhee, J.: Interannual and seasonal variability of snow depth scaling behavior
800 in a subalpine catchment, Water Resour Res, 56, e2020WR027343, 2020a.
801 Mendoza, P. A., Shaw, T. E., McPhee, J., Musselman, K. N., Revuelto, J., and
802 MacDonell, S.: Spatial distribution and scaling properties of lidar-derived snow depth
803 in the extratropical Andes, Water Resour Res, 56, e2020WR028480, 2020b.
804 Painter, T. H., Berisford, D. F., Boardman, J. W., Bormann, K. J., Deems, J. S.,
805 Gehrke, F., Hedrick, A., Joyce, M., Laidlaw, R., and Marks, D.: The Airborne Snow
806 Observatory: Fusion of scanning lidar, imaging spectrometer, and physically-based
807 modeling for mapping snow water equivalent and snow albedo, Remote Sens Environ,
808 184, 139–152, 2016.
809 Palomaki, R. T. and Sproles, E. A.: Assessment of L-band InSAR snow estimation
810 techniques over a shallow, heterogeneous prairie snowpack, Remote Sens Environ,
811 296, 113744, 2023.
812 Pflug, J. M., Wrzesien, M. L., Kumar, S. V, Cho, E., Arsenault, K. R., Houser, P.
813 R., and Vuyovich, C. M.: Extending the utility of space-borne snow water equivalent
814 observations over vegetated areas with data assimilation, Hydrol Earth Syst Sci, 28,
815 631–648, 2024.
816 Proksch, M., Mätzler, C., Wiesmann, A., Lemmetyinen, J., Schwank, M., Löwe,
817 H., and Schneebeli, M.: MEMLS3&a: Microwave Emission Model of Layered
818 Snowpacks adapted to include backscattering, Geosci Model Dev, 8, 2611–2626,

819 2015.

820 Rosen, P. A., Hensley, S., Wheeler, K., Sadowy, G., Miller, T., Shaffer, S.,
821 Muellerschoen, R., Jones, C., Zebker, H., and Madsen, S.: UAVSAR: A new NASA
822 airborne SAR system for science and technology research, in: 2006 IEEE conference
823 on radar, 8-pp, 2006.

824 Ruiz, J. J., Lemmetyinen, J., Kontu, A., Tarvainen, R., Vehmas, R., Pulliainen, J.,
825 and Praks, J.: Investigation of environmental effects on coherence loss in SAR
826 interferometry for snow water equivalent retrieval, IEEE Transactions on Geoscience
827 and Remote Sensing, 60, 1–15, 2022.

828 Shrestha P. and A . P. Barros: Multi-physics Data Assimilation Framework for
829 Remotely Sensed Snowpacks to Improve Water Prediction, Water Resource
830 Research, 2024.

831 Shrestha, P. and Barros, A. P.: Multi-physics data assimilation framework for
832 remotely sensed Snowpacks to improve water prediction, Water Resour Res, 61,
833 e2024WR037885, 2025.

834 Singh, S., Durand, M., Kim, E., and Barros, A. P.: Bayesian physical–statistical
835 retrieval of snow water equivalent and snow depth from X-and Ku-band synthetic
836 aperture radar–demonstration using airborne SnowSAr in SnowEx'17, Cryosphere, 18,
837 747–773, 2024.

838 Smith, E. K. and Weintraub, S.: The constants in the equation for atmospheric
839 refractive index at radio frequencies, Proceedings of the IRE, 41, 1035–1037, 1953.

840 Tarricone, J., Webb, R. W., Marshall, H.-P., Nolin, A. W., and Meyer, F. J.:
841 Estimating snow accumulation and ablation with L-band InSAR, The Cryosphere
842 Discussions, 2022, 1–33, 2022.

843 Tsang, L., Durand, M., Derksen, C., Barros, A. P., Kang, D.-H., Lievens, H.,
844 Marshall, H.-P., Zhu, J., Johnson, J., and King, J.: Global monitoring of snow water

845 equivalent using high frequency radar remote sensing, The Cryosphere Discussions,
846 2021, 1–57, 2021.
847 Vuyovich, C., H.P. Marshall, K. Elder, C. Hiemstra, L. Brucker, and M. McCormick:
848 SnowEx20 Grand Mesa Intensive Observation Period Snow Pit Measurements,
849 Version 1, NASA National Snow and Ice Data Center Distributed Active Archive Center,
850 2021.
851 Wang, X., Zeng, Q., and Jiao, J.: Utilization of WRF 3D Meteorological Data to
852 Calculate Slant Total Delay for InSAR Atmospheric Correction, Remote Sens Earth
853 Syst Sci, 4, 30–43, 2021.
854 Wiesmann, A. and Mätzler, C.: Microwave emission model of layered snowpacks,
855 Remote Sens Environ, 70, 307–316, 1999.
856 Xia, Y., Mitchell, K., Ek, M., Cosgrove, B., Sheffield, J., Luo, L., Alonge, C., Wei,
857 H., Meng, J., and Livneh, B.: Continental-scale water and energy flux analysis and
858 validation for North American Land Data Assimilation System project phase 2 (NLDAS-
859 2): 2. Validation of model-simulated streamflow, Journal of Geophysical Research:
860 Atmospheres, 117, 2012a.
861 Xia, Y., Mitchell, K., Ek, M., Sheffield, J., Cosgrove, B., Wood, E., Luo, L., Alonge,
862 C., Wei, H., and Meng, J.: Continental-scale water and energy flux analysis and
863 validation for the North American Land Data Assimilation System project phase 2
864 (NLDAS-2): 1. Intercomparison and application of model products, Journal of
865 Geophysical Research: Atmospheres, 117, 2012b.
866
867

Appendix A1

The atmospheric delay experienced by a microwave signal can be estimated by integrating the atmospheric refractivity along the line of sight from the surface to the airborne sensor height. Neglecting the impact of ionosphere for the UAVSAR flying at a height of z_s, the scaled up atmospheric refractivity of moist air [N=(n-1)10^6], where n is the refractive index, is given by

$$N(x,z) = k_1 \frac{P}{T} + (k_2 - k_1)\frac{e}{T} + k_3 \frac{e}{T^2} + k_4 W_{cl}$$

where P is pressure [hPa], T is air temperature [K], e is vapor pressure [hPa], W_{cl} is liquid water content [kgm^{-3}], n_e is ionization and f is frequency. The remaining term are constants: $k_1 = 0.776\, KPa^{-1}$, $k_2 = 0.716\, KPa^{-1}$, $k_3 = 3750\, K^2 Pa^{-1}$, $k_4 = 1430\, m^3 kg^{-1}$. Based on the works of Smith and Weintraub (1953), the above relation is restricted to certain limits of the variables for an accuracy of 0.5 percent in N(x,z). The limits in this case restrict its use to temperatures of -50 to + 40° C, total pressures of 200 to 1100 mb, water-vapor partial pressures of 0 to 30 mb, and a frequency range of 0 to 30 GHz.

$N(x,z)$ can be further decomposed into the mean and turbulent part for a radar scene as:

$$N(x,z) = \bar{N}(z) + N'(x,z)$$

where $\bar{N}(z)$ is the average vertical stratification for the given resolution of the atmospheric model (here 3 km) and $N'(x,z)$ is the deviation from the average profile along the location x in the radar scene (within the atmospheric grid). Neglecting the turbulent terms, zenith delay L for the mean part can be computed as

$$L = \int_{z_{ref}}^{z_s} \left(k_1 \frac{P}{T} + (k_2 - k_1)\frac{e}{T} + k_3 \frac{e}{T^2} \right) dz$$

Using $dP = -\rho g dz$ and $\rho = P/R_d T$, where ρ is air density [kgm^{-3}] , $R_d =$

893 $287.053\,Jkg^{-1}K^{-1}$ is the dry gas constant, ang g is acceleration due to gravity, we
894 obtain:

895 $$L = -10^{-6}\left(k_1\frac{R_d}{g}\left(P(z_s) - P(z_{ref})\right)\right) + 10^{-6}\int_{z_{ref}}^{z_s}\left((k_2 - k_1)\frac{e}{T} + k_3\frac{e}{T^2}\right)dz$$

896 The first term of the right side is the hydrostatic correction term, and the second
897 term is the wet correction term. The atmospheric phase delay along the line of sight
898 (LOS) can then be estimated using the microwave wavelength (λ) and incidence angle
899 (θ_{inc}) as:

900 $$\emptyset_{atm} = \frac{4\pi}{\lambda}\frac{L}{\cos(\theta_{inc})}$$

901 The above simple approximation for computing atmospheric phase delay along
902 the LOS could introduce additional uncertainty(Wang et al., 2021). More importantly,
903 since SAR interferograms are not sensitive to image-wide phase biases, there will be
904 no horizontal delay differences over flat terrain. However, for a radar scene with terrain,
905 the differences in the vertical refractivity during both acquisitions will affect phase
906 difference between two arbitrary resolution cells with different topographic
907 height(Hanssen, 2001). Therefore, the contribution of tropospheric stratification in the
908 interferogram will only be present if the radar scene has resolution cells with different
909 elevations. So, we compute the differential atmospheric phase delay between location
910 with maximum elevation ($z_{ref} = p$) and all other locations ($z_{ref} = q$) in the radar scene
911 for two SAR acquisition time t_1 and t_2 as:

912 $$\Delta\emptyset_{atm} = \frac{4\pi}{\lambda cos\theta_{inc}}\left[(L_p^{t_1} - L_q^{t_1}) - (L_p^{t_2} - L_q^{t_2})\right]$$

913 Then the phase change contribution due to snowpack is estimated as:

914 $$\Delta\emptyset_s = \Delta\emptyset_{InSAR} - \Delta\emptyset_{atm}$$

915

Tables

Table 1: UAVSAR flight retrieval dates for Grand Mesa during SnowEx'20 campaign.

Flight track	Acquisition Date
3	Feb 01 2020 (02:13:36 – 02:15:58 UTC)
5	Feb 12 2020 (16:47:20 – 16:49:45 UTC)
8	Feb 19 2020 (17:24:18 – 17:27:07 UTC)
13	Feb 26 2020 (17:40:54 – 17:43:34 UTC)
17	Mar 12 2020 (18:17:08 – 18:20:28 UTC)

Table 2: Coherence for treeless and forested environment for different retrievals.

	Period (days)	Coherence (HH)	
		Treeless	Forested
Feb 12-19	7	0.71 ± 0.15	0.65 ± 0.18
Feb 19-26	7	0.6 ± 0.18	0.5 ± 0.2
Feb 1-12	11	0.48 ± 0.18	0.47 ± 0.19
Feb 26 – Mar 12	15	0.49 ± 0.17	0.39 ± 0.18
Feb 1-19	18	0.47 ± 0.18	0.43 ± 0.19
Feb 1-26	25	0.46 ± 0.18	0.43 ± 0.18
Feb 1- Mar 12	40	0.39 ± 0.16	0.36 ± 0.17

Table 3: InSAR retrievals of snow depth change at different polarization for Feb 1-12

Polariation	Coherence	% missing	Avg. Change (cm)
VV	0.51	8	-1.13
HH	0.46	11	-0.1
HV	0.39	36	2.61
VH	0.39	54	-2.67

Table 4: Root mean square error for modeled snow depth (cm) over treeless environments with reference to pit (IOP and TSD) and snow pole measurements.

	Pit	W1A	W1B	W3A
CTRL	35.2	17.6	21.2	27.2
OL	36.0	11.57	14.80	30.8
DA	18.3	8.1	21	20.8
DAU	18.0	8.5	22.2	19.2

Figures

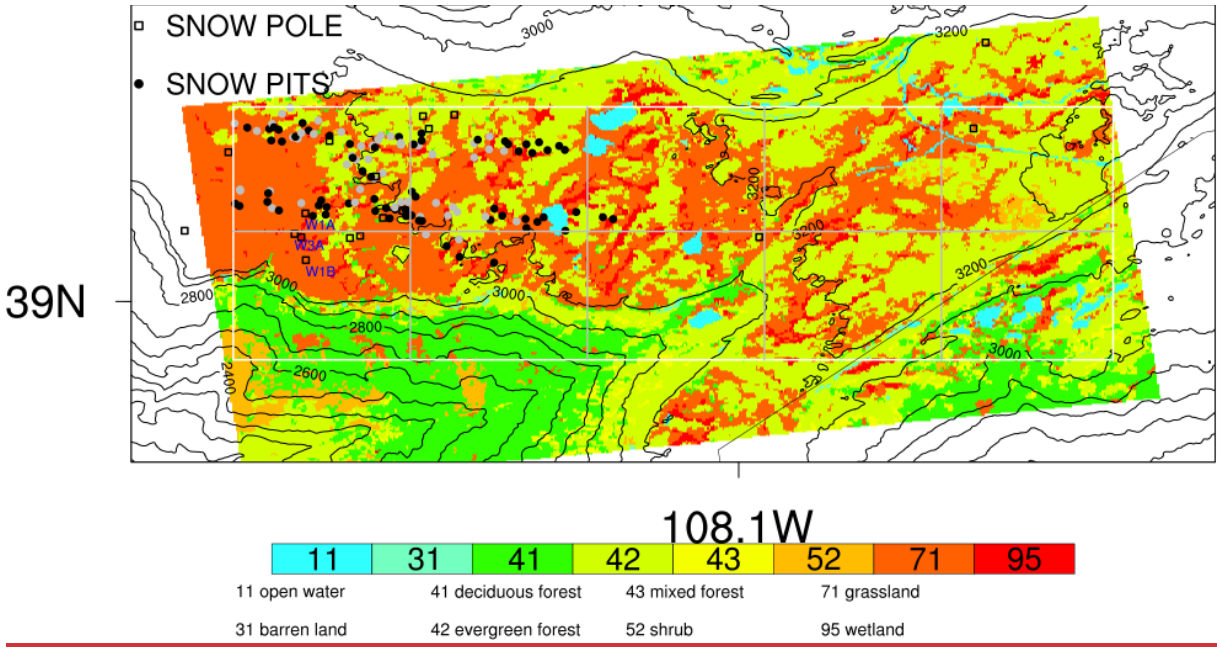

Figure 1: Spatial pattern of land cover and topography over the Grand Mesa (GM) domain (white outline). The gray boxes outline the 3 km atmospheric grids. The solid black/gray and square markers show the location of snow pit and snow pole measurements available from SnowEx'20 campaign. The snow pole measurements used for calibration of InSAR retrievals are also highlighted with their names.

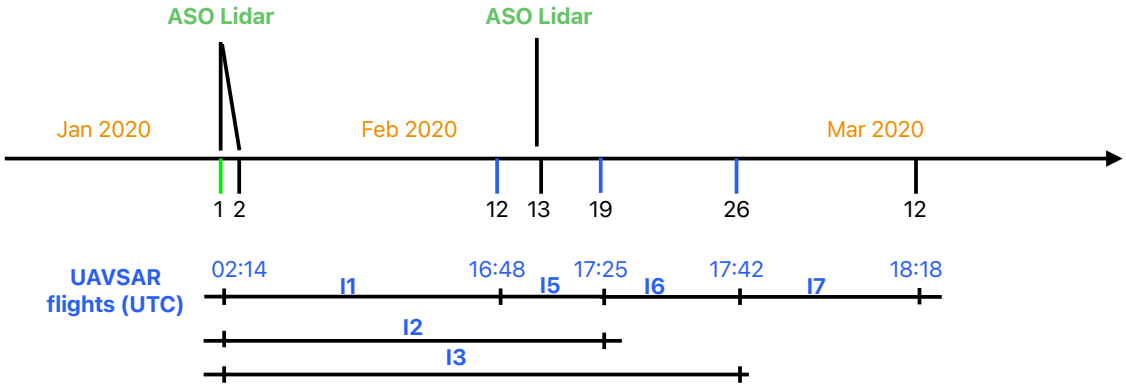

938

939 **Figure 2:** Timeline of availability of UAVSAR interferometric products and ASO Lidar
940 retrievals of snow depth and SWE for SnowEx'20 campaign over Grand Mesa. I1, I2,
941 I3 and I5, I6, I7 indicate the six InSAR pairs used for data assimilation and model
942 evaluation respectively. The dates with green and blue tick mark represent days when
943 the retrievals were used for assimilation in the data assimilation experiments.

944

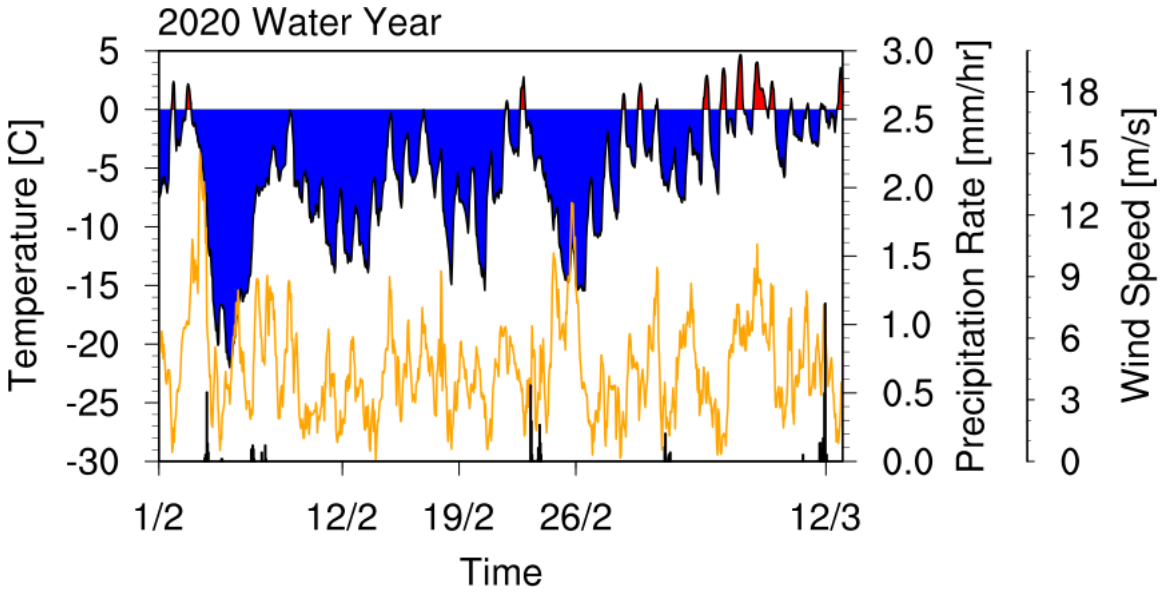

945

946 **Figure 3:** Meteorological data from atmospheric model for north-west GM subdomain
947 showing air temperature (blue/red), wind speed (orange) and precipitation rate (bar
948 plot). The time axis highlights the dates when the L-band UAVSAR flight data were
949 available for SnowEx'20 campaign.

950

951

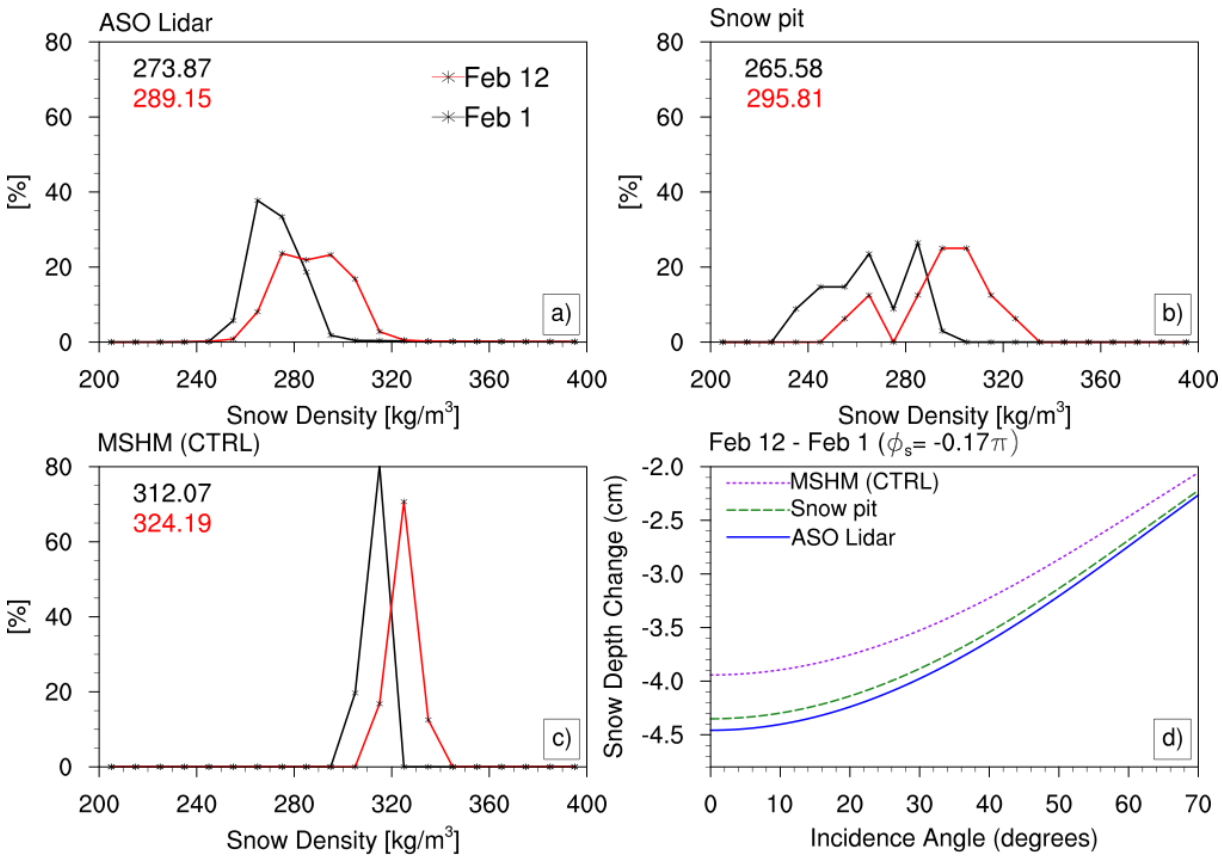

952

953

954 **Figure 4: a-c)** Snow density distribution ~~at two different dates~~on Feb 1 and Feb 12

955 from the ASO Lidar data, snow pit measurements (Intensive Observation Period, gray

956 solid markers in Fig. 1) and MSHM control run. **d)** Impact of snow density on the L-

957 band InSAR retrieval of snow depth change between the two dates as a function of

958 incidence angle for a fixed change in phase due to snowpack ($\emptyset_s = 0.17\pi$). The dates

959 for ASO Lidar in actual are Feb 1/2 and Feb 13. We use Feb 1 and Feb 12, due to

960 availability of InSAR phase data for these dates.

961

962

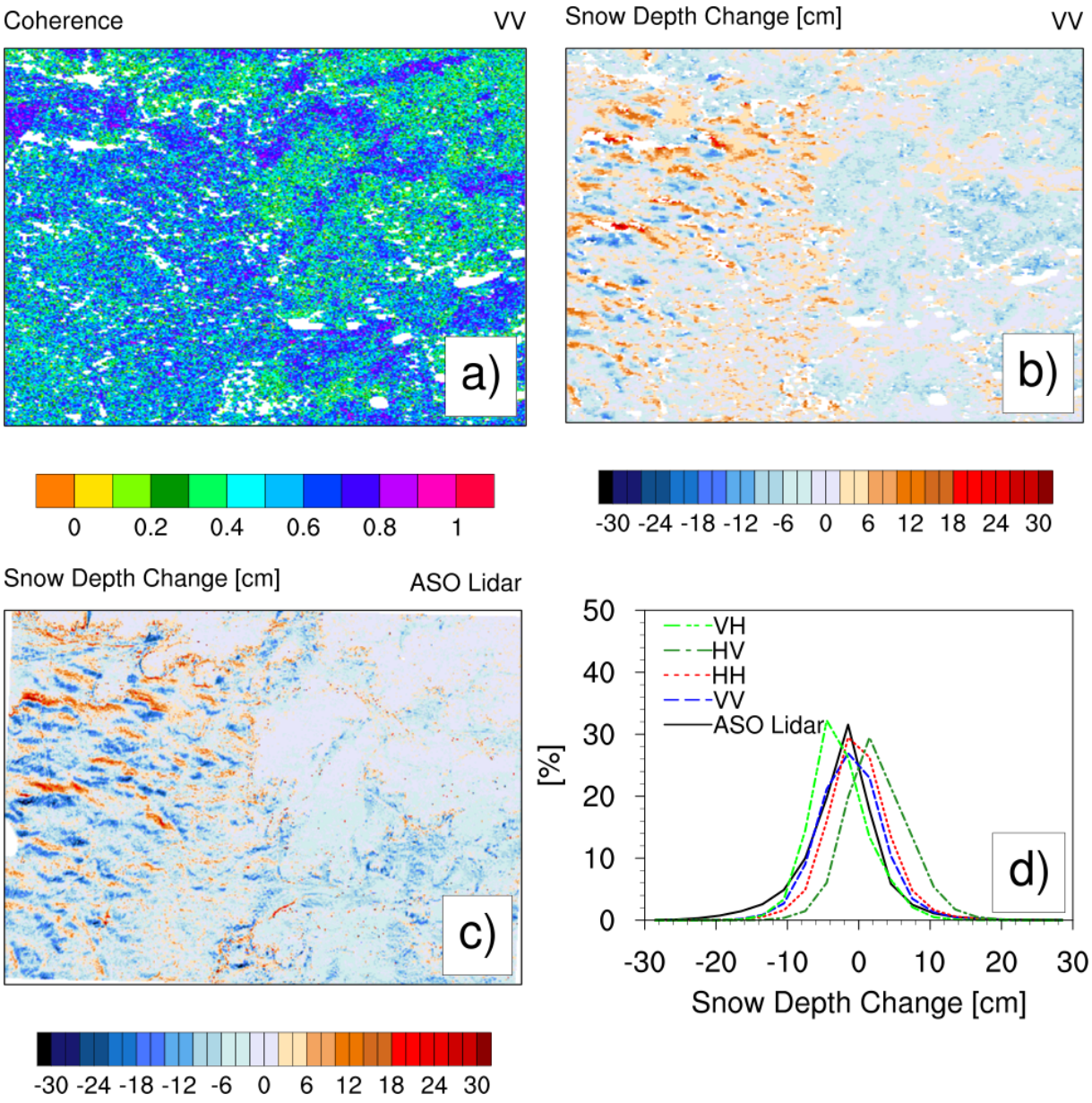

963

964

965 **Figure 5: a)** Spatial pattern of coherence from L-band VV polarization InSAR retrieval
966 for north-west GM subdomain. **b)** Estimated spatial pattern of snow depth changes
967 from the same retrieval. **c)** Spatial pattern of snow depth change from ASO Lidar data
968 (Feb 1/2–13). **d)** Distribution of change in snow depth for ASO Lidar and InSAR
969 retrievals for VV, HH, HV and VH polarizations. The InSAR retrievals were obtained
970 from UAVSAR flight pairs for Feb 1 and Feb 12.

971

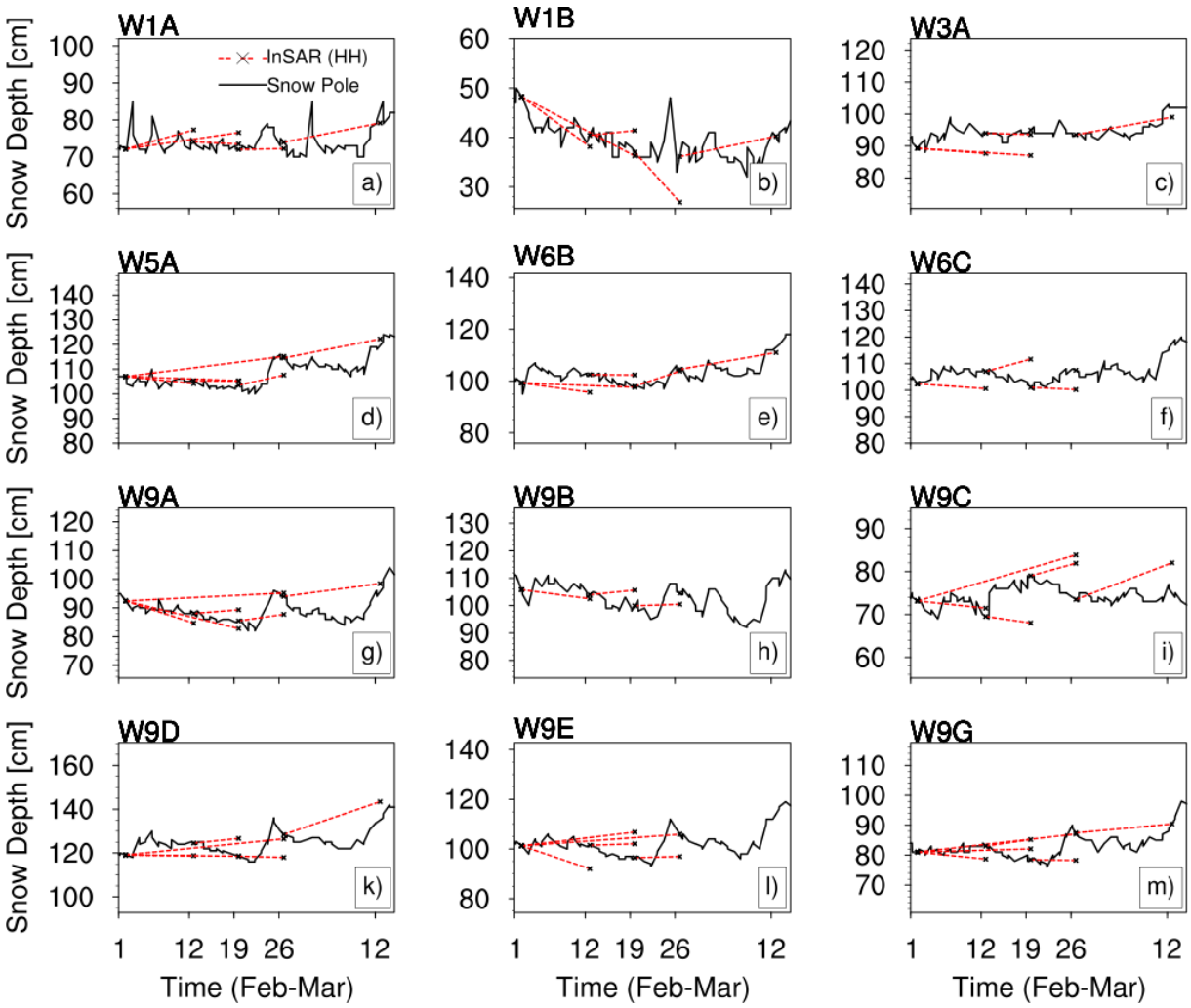

Figure 6: Comparison of L-band InSAR retrieval (HH polarization) of snow depth with Snow Pole measurements for locations with different landcover within the GM domain (**a-c:** Treeless; **d-f:** Sparse trees; **g-m:** Dense trees). For the InSAR retrieval, snow depth measurements from Snow Pole sites were used a reference for the repeat pass UAVSAR flight pairs.

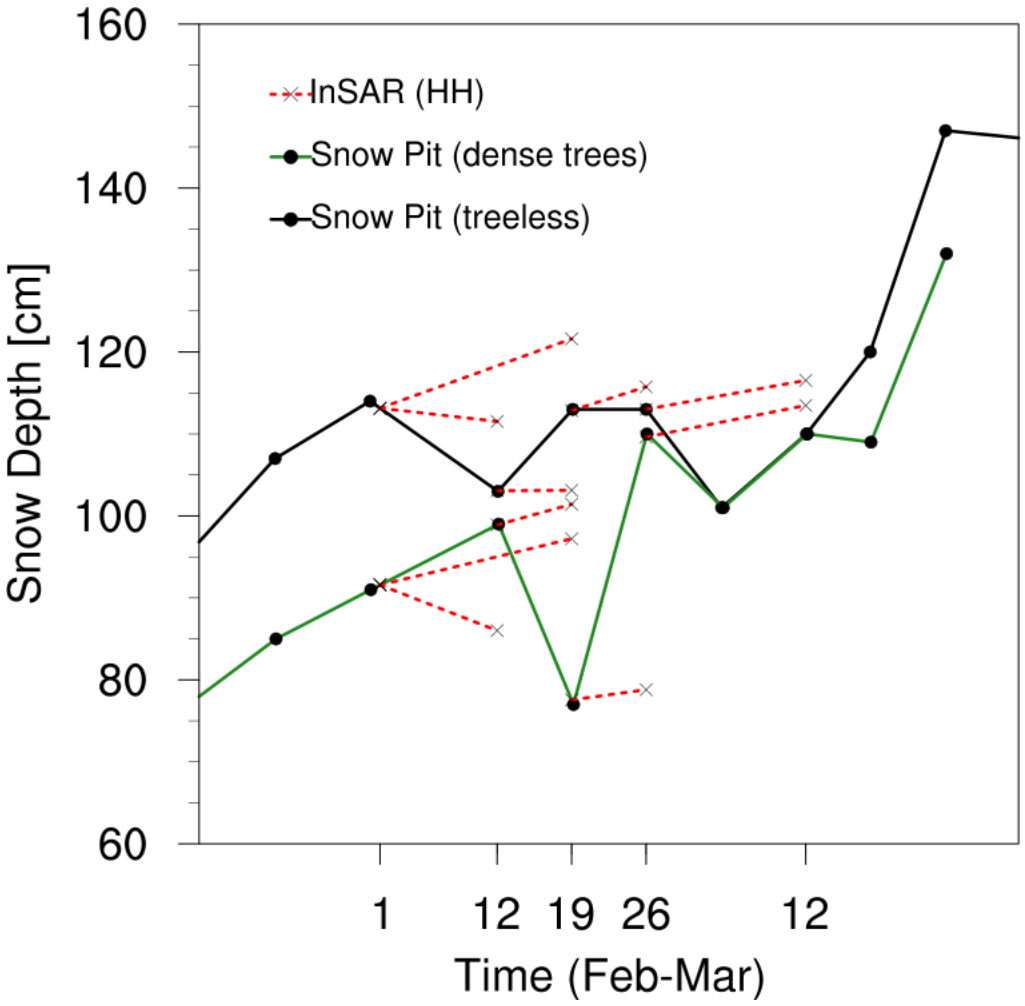

Figure 7: Comparison of L-band InSAR retrieval (HH polarization) of snow depth with snow pit time-series measurements for two locations with different landcover (treeless and dense trees) within the GM domain. For the InSAR retrieval, snow depth measurements from snow pit site were used a reference for the repeat pass UAVSAR flight pairs

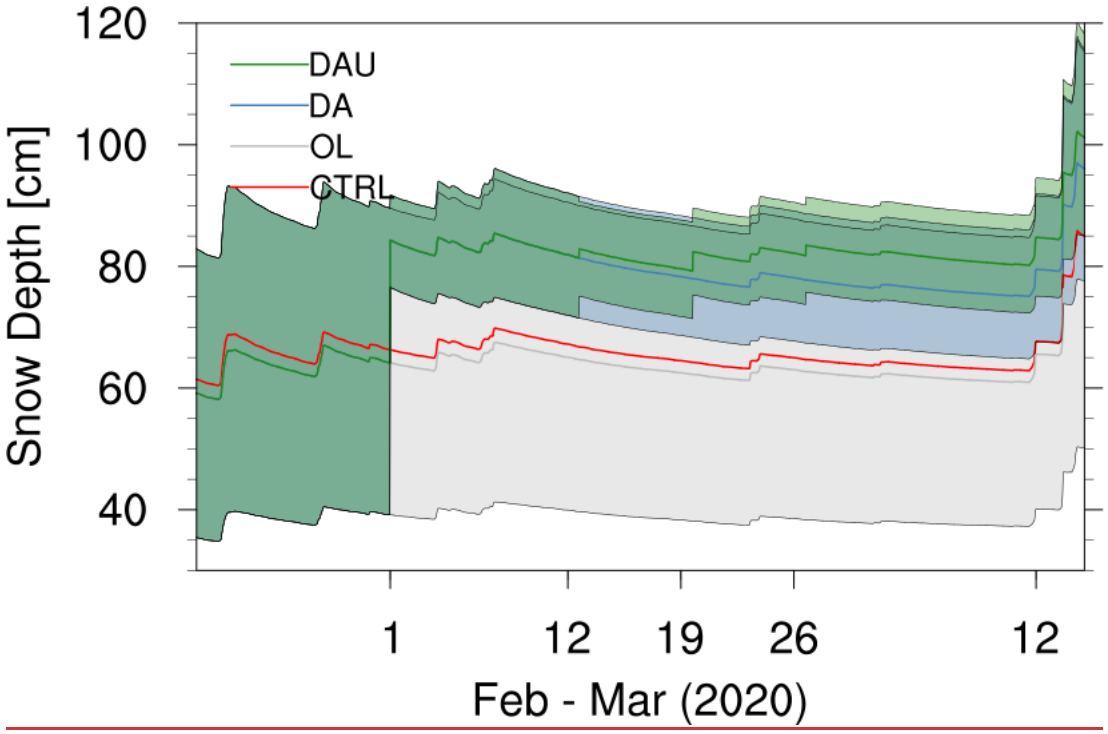

Figure 8: Time series of modeled snow depth for CTRL, OL, DA and DAU run. The dates when observation were assimilated are also shown by tick marks: DA (Feb 1) and DAU (Feb1, Feb 12 and Feb 26) are also shown by the tick marks. The ensemble spread for OL, DA and DAU runs are shown by the dotted lines.

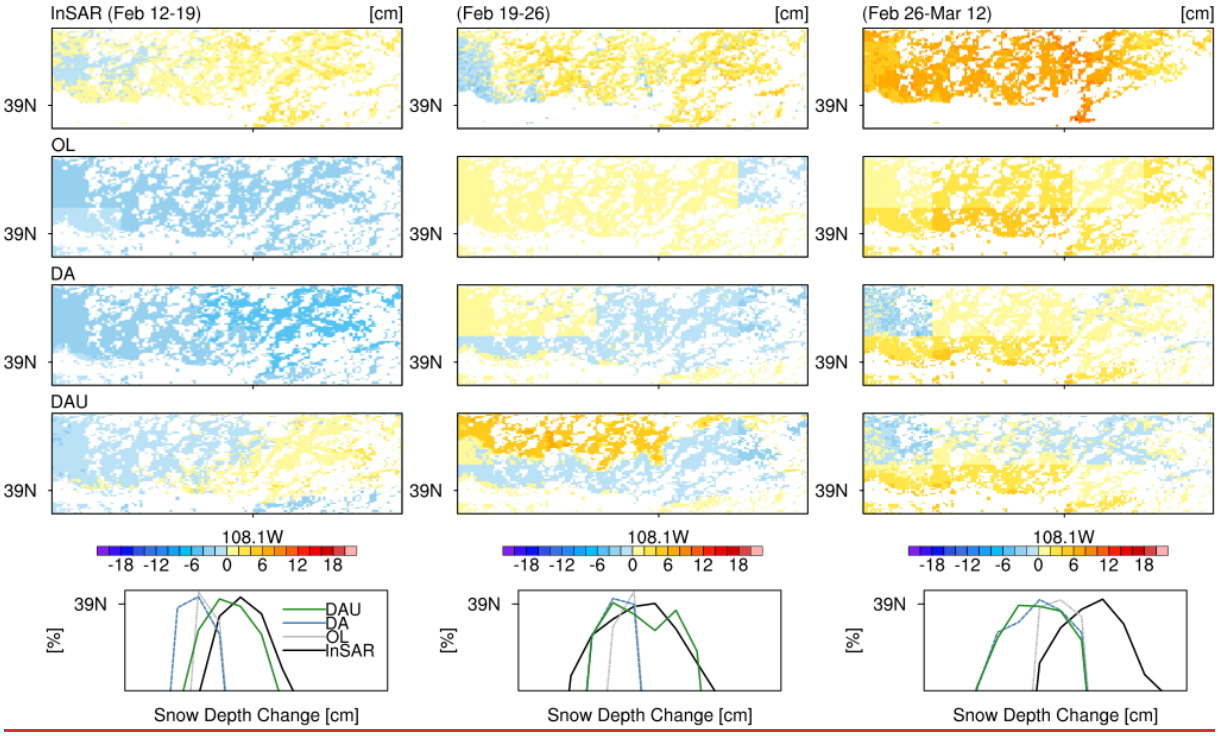

Figure 9: Spatial pattern and histogram of change in snow depth over the GM domain for Feb 12-19, Feb 19-26 and Feb 26-Mar 12: **a-c)** InSAR retrievals, **d-f)** ensemble averaged open loop run (OL), **g-i)** ensemble averaged data assimilation run with ASO Lidar data (DA), **j-l)** ensemble average data assimilation runs with ASO Lidar and referenced InSAR data (DAU), and **m-p)** frequency distribution of snow depth change for InSAR, OL, DA and DAU runs for respective pairs.